nature physics

SUPPLEMENTARY INFORMATION
https://doi.org/10.1038/s41567-018-0066-3

In the format provided by the authors and unedited.

Quantum non-demolition detection of an itinerant microwave photon

S. Kono[1]*, K. Koshino[2], Y. Tabuchi[1], A. Noguchi[1] and Y. Nakamura[1,3]*

[1]Research Center for Advanced Science and Technology (RCAST), University of Tokyo, Tokyo, Japan. [2]College of Liberal Arts and Sciences, Tokyo Medical and Dental University, Ichikawa, Japan. [3]Center for Emergent Matter Science (CEMS), RIKEN, Wako, Japan. *e-mail: s.kono@qc.rcast.u-tokyo.ac.jp; yasunobu@ap.t.u-tokyo.ac.jp

Supplementary Information for "Quantum non-demolition detection of an itinerant microwave photon"

S. Kono[1], K. Koshino[2], Y. Tabuchi[1], A. Noguchi[1], and Y. Nakamura[1,3]
[1] *Research Center for Advanced Science and Technology (RCAST), The University of Tokyo, Meguro-ku, Tokyo 153-8904, Japan*
[2] *College of Liberal Arts and Sciences, Tokyo Medical and Dental University, Ichikawa, Chiba 272-0827, Japan and*
[3] *Center for Emergent Matter Science (CEMS), RIKEN, Wako, Saitama 351-0198, Japan*

S1. EXPERIMENTAL SETUP

The experimental setup is shown in Fig. S1. We use a circuit-QED architecture, where a transmon qubit is mounted at the center of a three-dimensional superconducting cavity. The qubit with an Al/AlO$_x$/Al Josephson junction is fabricated on a sapphire substrate (5×5 mm). The cavity is made of aluminum (A1050) and has a single SMA-connector port connected with a coaxial cable. The cavity output is connected to a flux-driven Josephson parametric amplifier (JPA), which is fabricated on a silicon substrate (2.5×5 mm). The JPA enables us to read out the qubit state in a single shot by amplifying a readout signal nearly in the quantum limit. The system parameters are listed in Table S1.

These samples are cooled to $T \sim 50$ mK in a dilution refrigerator. The input and pump lines are highly attenuated to cut the background noise from the higher-temperature parts. A cryogenic HEMT amplifier is mounted at the 4-K stage in the output line together with a circulator to cut the backward noise from the amplifier. We also put circulators between the cavity and the JPA to protect the qubit coherence from amplified vacuum fluctuations generated by the JPA. The JPA resonance frequency is tuned to the cavity resonance frequency ω_c by applying a DC magnetic field into the SQUID loop. The JPA is pumped at $2\omega_c$ for the operation in the degenerate mode.

We use two different microwave sources, one for the qubit control at frequency ω_q, the other for the qubit read-

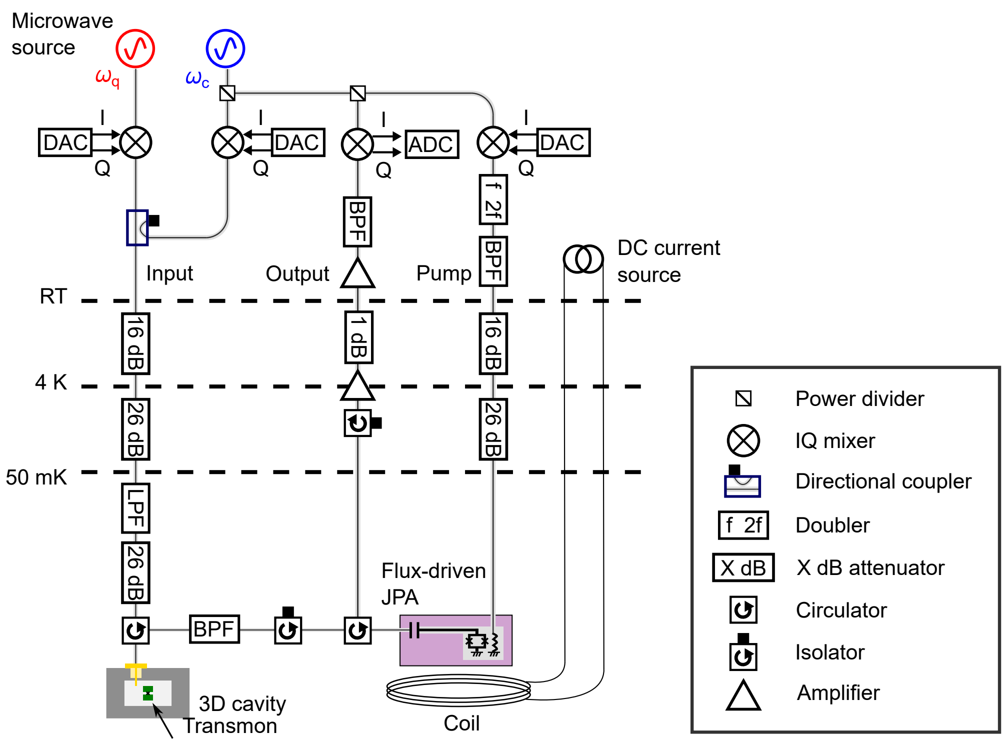

FIG. S1. Schematic of the experimental setup.

TABLE S1. System parameters.

Cavity resonant frequency	$\omega_c/2\pi$	10.62524 GHz
Cavity external coupling rate	$\kappa_{ex}/2\pi$	3.32 MHz
Cavity internal loss rate	$\kappa_{in}/2\pi$	0.25 MHz
Qubit resonant frequency	$\omega_q/2\pi$	7.8693 GHz
Qubit anharmonicity	$\alpha/2\pi$	−0.344 GHz
Qubit relaxation time	T_1	32 μs
Qubit dephasing time	T_2^*	26 μs
Qubit dephasing time (Echo)	T_{2E}	33 μs
Qubit thermal population	p_{th}	0.067
Dispersive shift	$\chi/2\pi$	1.50 MHz
JPA external coupling rate	$\kappa_{ex}^{J}/2\pi$	60 MHz
JPA internal loss rate	$\kappa_{in}^{J}/2\pi$	0.7 MHz
JPA gain	G	25 dB
JPA gain bandwidth	$B/2\pi$	1.4 MHz

out at frequency ω_c. Each continuous-wave carrier signal is modulated at an IQ mixer with a low-frequency signal (∼100 MHz), which is generated by a digital-to-analog converter (DAC) at 1-GHz sampling rate and filtered with a low-pass filter with a cut-off frequency of ∼100 MHz. The output signal is demodulated at an IQ mixer and measured with an analog-to-digital converter (ADC) at 1-GHz sampling rate. The In-phase and Quadrature-phase signals of an arbitrary temporal mode are extracted from the demodulated signals in the post analysis. Importantly, the identical microwave source is shared by the readout modulation, the pump modulation and the readout demodulation for the relative phase stability of the measurement.

The microwave source at ω_c is also used for the generation of an input state, a superposition of the vacuum and single-photon states in a pulse mode. The superposition is approximated by a weak coherent state, which is prepared and delivered to the cavity by attenuating a microwave pulse in the input line. For quantum state tomography of the reflected pulse mode, we use the same measurement chain as the qubit readout. A single quadrature of the pulse mode is amplified by the phase-sensitive amplifier (JPA), and is measured by the heterodyne voltage detector (IQ

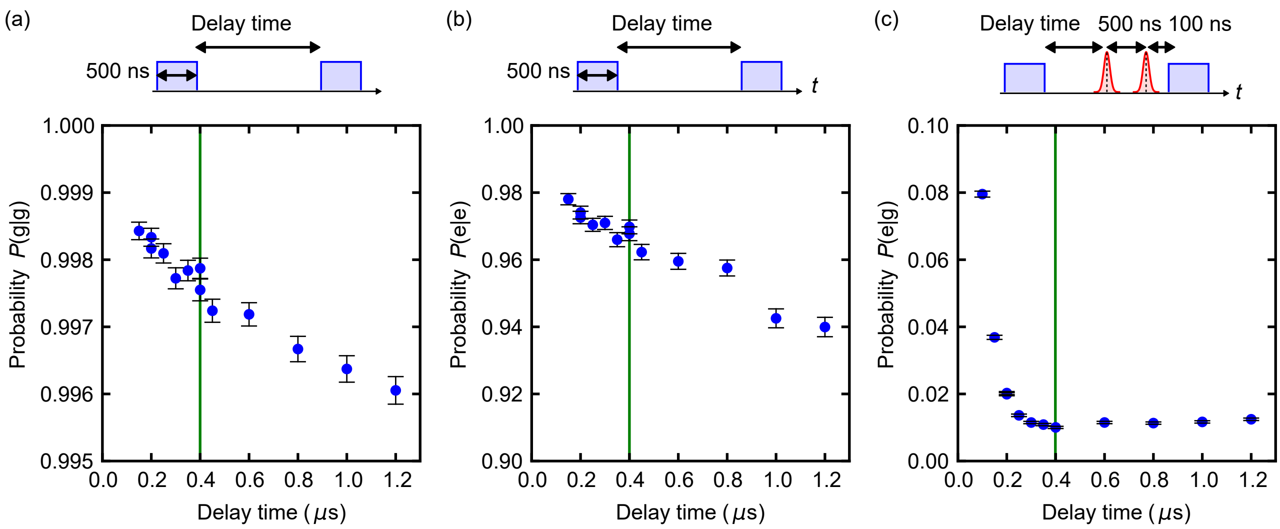

FIG. S2. Conditional probability $P(p|q)$ in the two successive qubit-state measurements ($p, q =$ g,e). The blue dots are the experimental results. The green vertical lines indicate the delay time we use in the QND detection. (a) Dependence of P(g|g) on the delay time between the two readouts. (b) The same for P(e|e). (c) Dependence of P(e|g) on the delay time of the Ramsey sequence from the first readout. The error bars on the data points are the standard deviations from the mean.

mixer and ADC). We achieve a high measurement efficiency $\eta_{\rm meas} = 0.43 \pm 0.01$, since a phase-sensitive amplifier amplifies one quadrature without adding any vacuum noise and suppress the influence of the propagation loss and the classical amplifier noise in the following stages (details below). Note that the temporal mode mismatch between the reflected pulse mode and the demodulation mode is critical in the quadrature measurement. Since the bandwidth of the input pulse mode is narrow enough compared to that of the cavity, we use the same temporal mode as the input pulse for the demodulation and match the timing to the reflected coherent pulse.

S2. SYSTEM INITIALIZATION AND QUBIT READOUT

To achieve a high quantum efficiency of the QND detection, the high-fidelity initialization of the system and the high-fidelity readout of the qubit state are of importance.

The transmission lines, connected to the cavity for both the input and output, are heavily attenuated to cut the thermal background noise from room temperature. We evaluate the average thermal photon number $n_{\rm th}$ in the cavity from the qubit echo dephasing rate $\gamma_{\phi{\rm E}} = \frac{1}{T_{\rm 2E}} - \frac{1}{2T_1}$. Supposing that the thermal photons are dominating the dephasing rate, the upper bound of the thermal average photon number in the cavity is determined to be $n_{\rm th}^{\rm max} = \frac{\kappa_{\rm tot}^2+\chi^2}{4\kappa_{\rm tot}\chi^2}\gamma_\phi^{\rm E} = 0.001$, where $\kappa_{\rm tot} = \kappa_{\rm ex} + \kappa_{\rm in}$ is the total cavity relaxation rate [1]. Considering the upper bound and taking the lower bound to be zero, we set $n_{\rm th} = 0.0005 \pm 0.0005$. When a Gaussian with the full width at half maximum of 500 ns is used as the input pulse mode, the reflected pulse mode in the absence of any input signal is in the thermal state with the average photon number $n_{\rm th}^{\rm P}$ of 0.004 ± 0.004, which is obtained by integrating the output thermal photon flux $\kappa_{\rm ex} n_{\rm th}$ with the same temporal mode as the input pulse.

We read out the qubit nondestructively via the dispersive shift of the cavity resonance frequency. We use a square pulse with the length of 500 ns for the readout. In Figs. S2(a) and (b), we show the correlation between the first and second readout outcomes as a function of the delay time between the two. At the delay time of 150 ns (the end time of the first pump pulse), we evaluate the assignment fidelity of $[P({\rm g|g}) + P({\rm e|e})]/2 = 0.988 \pm 0.001$. We also determine the upper bound of the readout error of the qubit in the ground state (excited state) to be $\varepsilon_{\rm r}^{\rm g} \leq 1 - P({\rm g|g}) = 0.0016$ $[\varepsilon_{\rm r}^{\rm e} \leq 1 - P({\rm e|e}) = 0.022]$, which are used for the numerical calculation (see Section. S7).

The population of the qubit excited state is $p_{\rm th} = 0.067 \pm 0.006$ in thermal equilibrium, which corresponds to the initialization fidelity of 0.933. To increase the fidelity, we initialize the qubit in the ground state by nondestructive readout of the qubit state and postselection. As shown in Fig. S2(a), the conditional probability $P({\rm g|g})$ is much larger than the initialization fidelity in the thermal equilibrium. For a longer delay time the correlation becomes weaker due to the thermalization of the qubit.

Next, we study the effect of the residual cavity photons after the readout. In Fig. S2(c), we plot the conditional probability $P({\rm e|g})$ as a function of the delay time of the Ramsey pulses, whose interval is fixed to 500 ns. The qubit is initialized in the ground state by postselection on the first outcome. For the delay time shorter than the cavity

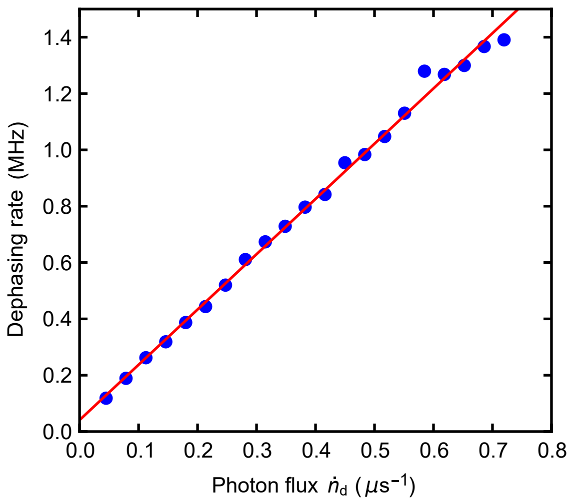

FIG. S3. Dephasing rate of the qubit as a function of the photon flux $\dot{n}_{\rm d}$ under the continuous coherent drive. The blue dots are the experimental results and the red line is the theoretical fit to calibrate the horizontal scale.

relaxation time $1/\kappa_{\mathrm{tot}}$, the photons excited by the readout pulse stay inside the cavity, causing the dephasing of the qubit. Therefore, the probability of finding the qubit in the excited state, resulting from the dephasing, is larger. The probability takes its minimum at the delay time of 400 ns, when both of the qubit and the cavity are initialized to the ground state. For longer delay times than 400 ns, the excitation probability becomes larger because the initialization infidelity increases due to the thermalization as shown in Fig. S2(a).

At the delay time of 400 ns the qubit is initialized to the ground state with the fidelity of 0.998 [Fig. S2(a)]. In the numerical calculation, the initialization infidelity of the qubit state is taken into account as a part of the readout errors (see Section. S7).

S3. CALIBRATION OF AVERAGE PHOTON NUMBER

To evaluate the quantum efficiency of the QND single-photon detection, we use a weak coherent state approximating a superposition of the vacuum and single-photon states. For the accurate evaluation, the power calibration of the coherent pulse is of importance. To determine the photon flux $\dot{n}_{\mathrm{d}}$ reaching the cavity, we measure the dephasing rate of the qubit in the cavity that is driven continuously with coherent microwaves. The dephasing rate of the qubit as a function of the photon flux $\dot{n}_{\mathrm{d}}$ of a continuous coherent drive is shown in Fig. S3, where the cavity-drive frequency ω_{d} is fixed closely to the cavity resonance frequency ω_{c}. Theoretically, the cavity-drive-induced dephasing rate is described by

$$\Gamma_{\mathrm{m}} = \frac{\kappa_{\mathrm{tot}}\chi^2}{\kappa_{\mathrm{tot}}^2/4 + \chi^2 + \Delta_{\mathrm{d}}^2}(\overline{n}_+ + \overline{n}_-), \tag{S1}$$

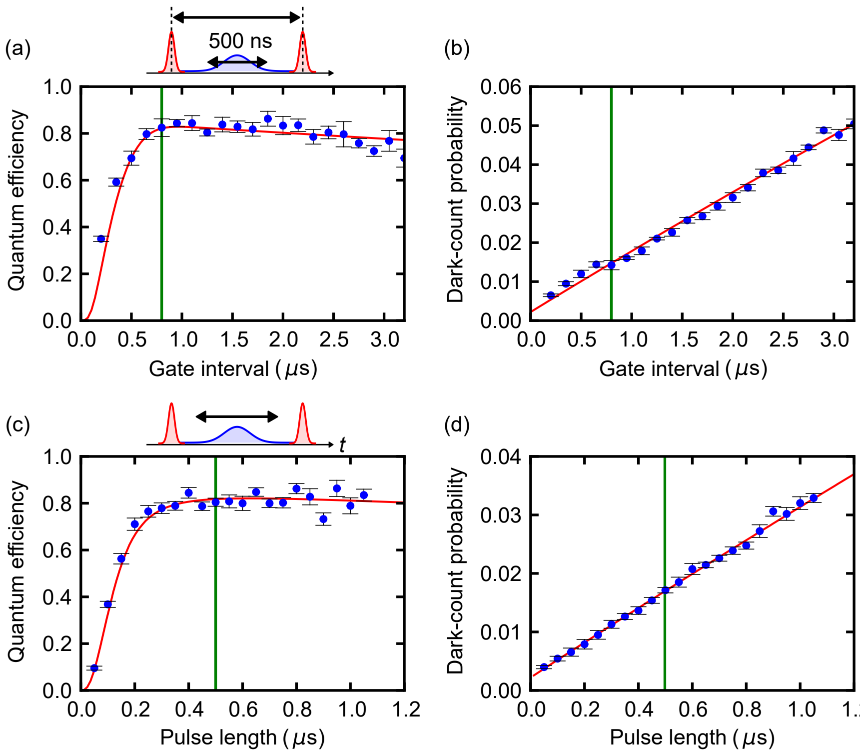

FIG. S4. Optimization of QND detection. (a), (b) Gate interval dependence of the quantum efficiency and the dark-count probability. (c), (d) Pulse length (FWHM) dependence of the quantum efficiency and the dark-count probability. The blue dots are the experimental results and the red lines are the numerical calculations without free parameters. The error bars on the data points include the fitting error and the uncertainty of the input average photon number. We determine the qubit pure dephasing rate γ_ϕ by fitting the dark-count probability. The value of γ_ϕ slowly fluctuates by $\sim 10\%$ in the time scale of a few days. The green vertical lines indicate the gate interval and the pulse length we use in the QND detection experiment in the main text, respectively.

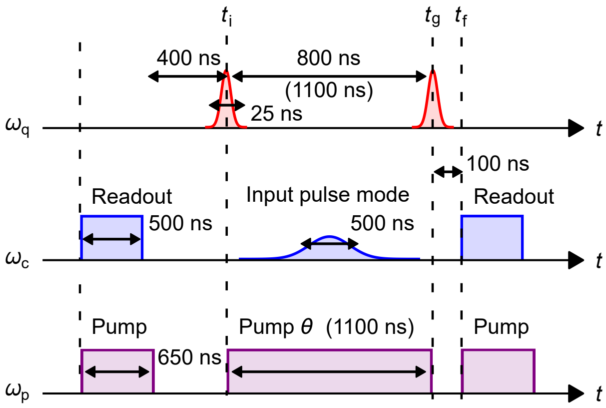

FIG. S5. Optimized pulse sequence for the QND detection of an itinerant single photon. The interval between the $\pi/2$-gates are 800 ns for the evaluation of the quantum efficiency and 1100 ns for the quantum state tomography of the reflected pulse mode. t_i is the initial time, t_g is the second gate time, and t_f is the measurement time in the numerical calculation (see Section S7).

where $\Delta_\mathrm{d} = \omega_\mathrm{d} - \omega_\mathrm{c} = 0.16$ MHz is the detuning, and $\overline{n}_\pm = \frac{\kappa_\mathrm{ex}\dot{n}_\mathrm{d}}{\kappa_\mathrm{tot}^2/4+(\Delta_\mathrm{d}\pm\chi)^2}$ is the average photon number in the cavity with the qubit in the ground state or in the excited state [2]. By comparing the slope (red line in Fig. S3) of the experimental results with Eq. (S1), we calibrate the photon flux $\dot{n}_\mathrm{d}$. We characterize the coherent state in the input pulse mode by calculating the average photon number in the temporal mode from the photon flux $\dot{n}_\mathrm{d}$.

S4. OPTIMIZATION OF QND DETECTION

We optimize the interaction between the qubit and the pulse mode in terms of the quantum efficiency of the QND detection. As shown in Fig. 2(c) in the main text, the quantum efficiency and the dark-count probability are determined by measuring the phase-flip probability as a function of the average photon number $|\alpha_\mathrm{in}|^2$ in the input pulse mode. The quantum efficiency is determined by fitting the result with the quadratic function and evaluating the differential coefficient at $|\alpha_\mathrm{in}|^2 = 0$. The dark-count probability corresponds to the phase-flip probability in the absence of any input signal.

First, the $\pi/2$-gate interval is optimized as shown in Figs. S4(a) and (b), where a coherent Gaussian pulse with the pulse length (the full width at half maximum in amplitude) of 500 ns is used as an input. The bandwidth of the input pulse is narrow enough to be reflected by the cavity without noticeable temporal/spectral mode distortion. When the gate interval is shorter than the input-pulse length, the quantum efficiency is reduced. The quantum efficiency increases up to the gate interval comparable with the pulse length, and then decreases for a gate interval longer than the pulse length. The longer the gate interval, the more phase-flip error due to dephasing occurs, resulting in the decrease of the quantum efficiency. From the experiment, we determine the optimized gate interval of 800 ns for the input-pulse length of 500 ns.

Next, we study the input-pulse length dependence of the quantum efficiency and the dark-count probability [Figs. S4(c) and (d)]. The gate interval is set to be proportional to the pulse length. Since the bandwidth in which the reflected pulse mode acquires the phase flip corresponds to that of the cavity, the qubit cannot detect efficiently a single photon with a larger bandwidth. A single photon with a narrow bandwidth interacts with the qubit ideally, while the longer gate interval causes the dephasing of the qubit, resulting in the decrease of the quantum efficiency again. In the experiment presented in the main text, we use a coherent Gaussian pulse with the pulse length of 500 ns [Figs. S4(c) and (d)].

Finally, we show the optimized pulse sequence for the QND detection of an itinerant photon in Fig. S5. The gate interval is set to 800 ns for the evaluation of the quantum efficiency and the dark-count probability, and is set to 1100 ns for quantum state tomography of the reflected pulse mode so that the second readout pulse does not interfere with the reflected pulse mode.

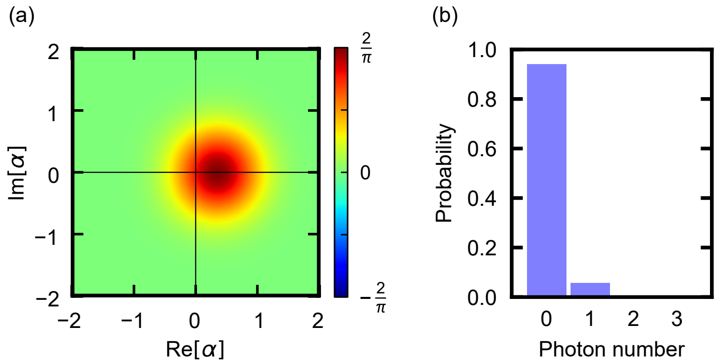

FIG. S6. Calibration of the quadrature measurement efficiency. (a),(b) Wigner function and photon-number distribution of the quantum state of the reflected pulse mode. The quantum state is a coherent state with the average photon number of 0.058.

S5. CALIBRATION OF QUADRATURE MEASUREMENT EFFICIENCY

To perform quantum state tomography of the reflected pulse mode, we use the iterative maximum likelihood reconstruction with correction for the measurement inefficiency $1-\eta_{\mathrm{meas}}$ of the quadrature measurement. Therefore, it is crucial to calibrate η_{meas} precisely. As described in Section S1, we measure a single quadrature of the reflected pulse mode in the nearly-quantum limit with a phase-sensitive amplifier and a heterodyne voltage detector. The effect of the residual propagation loss and Gaussian noise in the measurement chain can be modeled with the insertion of a beam splitter of transmittance η_{meas} in front of an ideal single quadrature detector[3]. To calibrate η_{meas}, we measure a coherent state in the pulse mode reflected by the cavity with the qubit being in the ground state. An input coherent state before the reflection is calibrated by the qubit dephasing induced by a coherent drive (See Section S3). We denote the average photon number in the input coherent pulse as $n_{\mathrm{in}} = |\alpha_{\mathrm{in}}|^2 = \int d\omega\ n_{\mathrm{in}}(\omega)$, where $n_{\mathrm{in}}(\omega)$ is the input average photon number per unit frequency. Furthermore, the cavity parameters are determined from independent measurements. Thus, the output coherent state in the reflected pulse mode can also be characterized. Denoting the average photon number in the reflected pulse as n_{out}, we derive from the input-output theory

$$n_{\mathrm{out}} = \int d\omega\, \frac{\frac{(\kappa_{\mathrm{ex}}-\kappa_{\mathrm{in}})^2}{4} + [\omega-(\omega_{\mathrm{c}}+\chi)]^2}{\frac{(\kappa_{\mathrm{ex}}+\kappa_{\mathrm{in}})^2}{4} + [\omega-(\omega_{\mathrm{c}}+\chi)]^2}\, n_{\mathrm{in}}(\omega). \tag{S2}$$

In the experiment, we use an input coherent pulse with $n_{\mathrm{in}} = 0.165 \pm 0.003$. Therefore, from Eq. (S2) we obtain $n_{\mathrm{out}} = 0.137 \pm 0.003$. The reflected pulse captured by the measurement chain is determined by the iterative maximum likelihood reconstruction without correcting for any inefficiency. The Wigner function and the photon-number distribution of the determined quantum state are shown in Fig. S6. The reflected pulse mode is in a coherent state with the average photon number $n'_{\mathrm{out}} = 0.058$, with the fidelity of 0.998. If the measurement chain of the quadrature is perfect, n'_{out} should be identical to n_{out}. However, it is not the case in the experiment because of the detection inefficiency $\widetilde{\eta}_{\mathrm{meas}}$. By comparing these average photon numbers, we calibrate the detection inefficiency as $\widetilde{\eta}_{\mathrm{meas}} = n'_{\mathrm{out}}/n_{\mathrm{out}} = 0.426 \pm 0.009$.

Here, the measurement efficiency $\widetilde{\eta}_{\mathrm{meas}}$ is affected by the imperfection in the initialization of the pulse mode, which leads to the overestimation of the photon number in the reflected pulse mode by the quantum state tomography with the correction. Actually, the pulse mode in the absence of any input signal is supposed to be in the thermal state with the average photon number $n_{\mathrm{th}}^{\mathrm{P}}$ of 0.004 ± 0.004 (see section S2). The ratio of the vacuum fluctuation to the thermal fluctuation is interpreted as the measurement efficiency $\eta_{\mathrm{th}} = \frac{1/2}{1/2+n_{\mathrm{th}}} = \frac{1}{1+2n_{\mathrm{th}}}$. Therefore, the total measurement efficiency $\widetilde{\eta}_{\mathrm{meas}}$ is described by $\eta_{\mathrm{th}}\eta_{\mathrm{meas}}$, where η_{meas} is the actual measurement efficiency of the reflected pulse mode. Using this, we determine $\eta_{\mathrm{meas}} = \widetilde{\eta}_{\mathrm{meas}}/\eta_{\mathrm{th}}$ to be 0.43 ± 0.01.

S6. RAW DATA ANALYSIS

In the main text, to evaluate the quantum state of the system, we corrected for the detection inefficiency $1-\eta_{\mathrm{meas}}$ in the quadrature analysis of the reflected pulse mode. Here, we show the evaluation using the raw data. The quantum

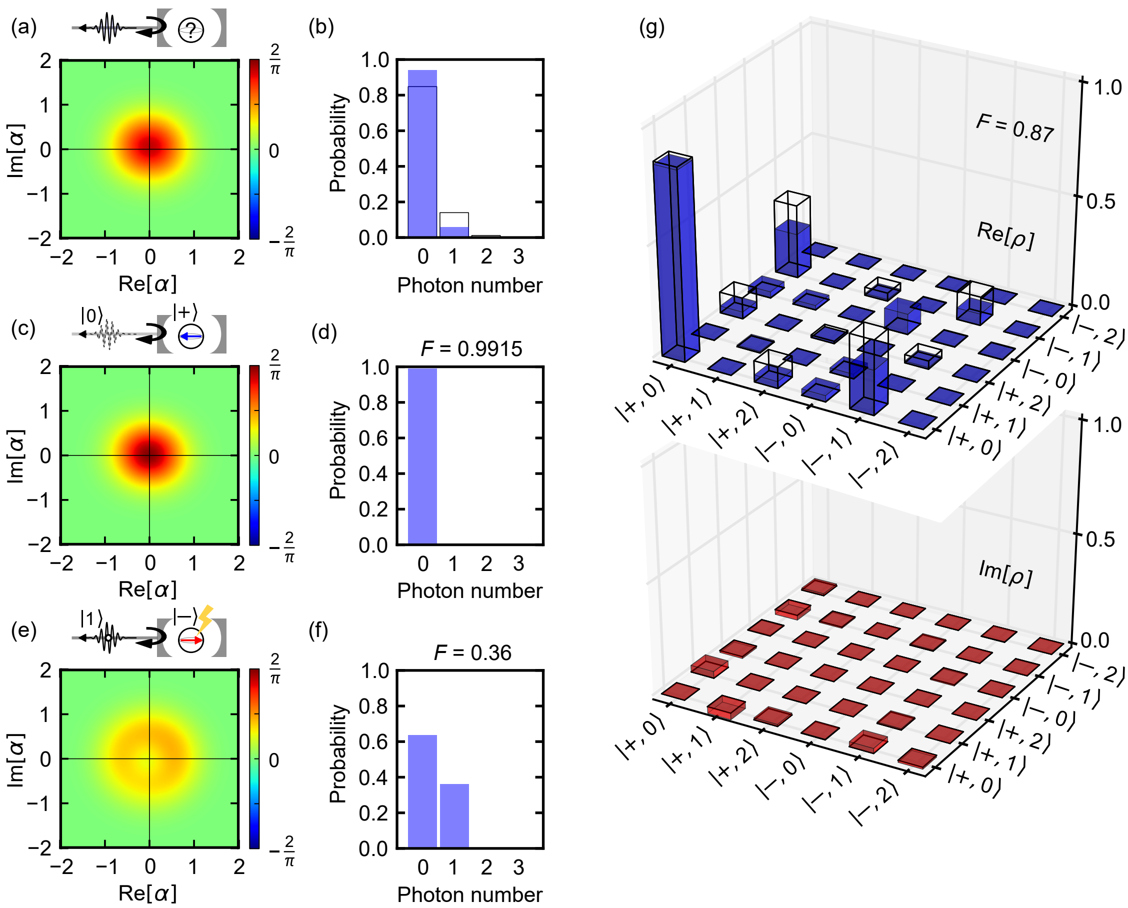

FIG. S7. Raw data analysis. (a), (b) Unconditional Wigner function and photon-number distribution of the reflected pulse mode after the interaction with the qubit prepared in the state $|+\rangle$. The blue bars in d shows the distribution in the reflected pulse, while the thin black frames depict that in the input pulse. (c), (d) The same conditioned on the absence of the qubit phase flip. (e), (f) The same conditioned on the detection of the qubit phase flip. (g) Qubit-photon entanglement. The blue and red bars respectively show the real and imaginary parts of the experimentally obtained density matrix of the composite system consisting of the qubit and the pulse mode. The black wireframes are the density matrix in the ideal case. The qubit state is represented in the X basis ($|+\rangle$, $|-\rangle$), and the state in the reflected pulse mode is represented in the photon-number basis ($|n\rangle$; n=0,1,2).

state is determined by the iterative maximum likelihood reconstruction without correcting the inefficiency [4]. In Figs. S7(a)-(f), we plot the Wigner function and the photon-number distribution of each quantum state in the reflected pulse mode. When the qubit remains in the state $|+\rangle$ after the interaction, the photon state is in the vacuum state $|0\rangle$ with a fidelity of 0.99. On the other hand, when the qubit acquires the phase flip to $|-\rangle$, the photon state is in the single photon state $|1\rangle$, with a fidelity of 0.36. The reduction of the fidelity is mainly due to the photon loss in the heterodyne measurement.

In Fig. S7(g), we show the determined density matrix of the composite system. We calculate the negativity of the composite system from the density matrix and obtain $\mathcal{N}(\rho) = 0.159 > 0$, quantitatively guaranteeing the presence of entanglement. The fidelity between the experiment and the ideal case is 0.87. The off-diagonal components are still observed in the density matrix with the raw data, which indicates the entanglement.

S7. THEORETICAL DESCRIPTION

A. Hamiltonian

The Hamiltonian describing the considered setup consists of three parts as

$$\mathcal{H} = \mathcal{H}_{\mathrm{sys}} + \mathcal{H}_{\mathrm{field}} + \mathcal{H}_{\mathrm{env}}, \tag{S3}$$

where $\mathcal{H}_{\mathrm{sys}}$, $\mathcal{H}_{\mathrm{field}}$, and $\mathcal{H}_{\mathrm{env}}$ respectively describe the qubit-cavity system, the interaction between the system and the pulse mode in the 1D transmission line, and the environmental degrees of freedom. Using the qubit operator $\sigma_{pq} = |p\rangle\langle q|$ ($p, q = \mathrm{g,e}$), $\mathcal{H}_{\mathrm{sys}}$ is given by (hereafter, $\hbar = 1$)

$$\mathcal{H}_{\mathrm{sys}} = (\omega_{\mathrm{c}} + \chi)a^\dagger a\sigma_{\mathrm{gg}} + [\omega_{\mathrm{q}} + (\omega_{\mathrm{c}} - \chi)a^\dagger a]\sigma_{\mathrm{ee}}, \tag{S4}$$

which is identical to Eq. (1) of the main text. The input/output port of the photon field is a semi-infinite transmission line field interacting with the cavity in reflection geometry. Setting the microwave velocity in the transmission line to unity, $\mathcal{H}_{\mathrm{field}}$ is given by

$$\mathcal{H}_{\mathrm{field}} = \int dk \left[ka_k^\dagger a_k + \sqrt{\kappa_{\mathrm{ex}}/2\pi}(a_k^\dagger a + a^\dagger a_k)\right], \tag{S5}$$

where a_k is the field annihilation operator with wave number k and κ_{ex} is cavity external coupling rate to this port. The field operator in the real-space representation is defined by $\widetilde{a}_r = (2\pi)^{-1/2}\int dk e^{ikr}a_k$. The environmental Hamiltonian $\mathcal{H}_{\mathrm{env}}$ involves other relaxation channels of the qubit and the cavity. The relevant parameters are κ_{in} (cavity internal loss rate), $n_{\mathrm{B}} = \frac{p_{\mathrm{th}}}{1+2p_{\mathrm{th}}}$ (average thermal quantum number of the qubit bath), $\gamma = \frac{1}{(1+2n_{\mathrm{B}})T_1}$ (qubit relaxation rate), and $\gamma_\phi = \frac{1}{T_2^*} - \frac{1}{2T_1}$ (qubit pure dephasing rate).

We model these dampings by the interaction with fictitious continuous fields similar to Eq. (S5). We omit their explicit forms here.

B. Initial state

The input pulse mode has a Gaussian envelope with the length (full width at half maximum in amplitude) l and the carrier frequency ω_{c}. Its mode function $f_{\mathrm{in}}(r)$ is given, in the real-space representation, by

$$f_{\mathrm{in}}(r) = \left(\frac{8\ln 2}{\pi l^2}\right)^{1/4} 2^{-(2r/l)^2} e^{i\omega_{\mathrm{c}} r}, \tag{S6}$$

which is normalized as $\int dr|f_{\mathrm{in}}(r)|^2 = 1$. We write the mode function in the time representation as $f_{\mathrm{in}}(-t)$, by setting the speed of light $c = 1$. The origin of the time coordinate t is chosen so that the photon amplitude entering the cavity becomes maximum at $t = 0$. Since the quantum state in the input pulse mode is a weak coherent state, its state vector $|\psi_{\mathrm{i}}\rangle$ at the initial moment $t = t_{\mathrm{i}}$ is written as

$$|\psi_{\mathrm{i}}\rangle = \mathcal{N}\exp\left(\alpha_{\mathrm{in}}\int dr f_{\mathrm{in}}(r - t_{\mathrm{i}})\widetilde{a}_r^\dagger\right)|\mathrm{vac}\rangle, \tag{S7}$$

where α_{in} is the amplitude of the input coherent state (average photon number $= |\alpha_{\mathrm{in}}|^2$), $|\mathrm{vac}\rangle$ is the vacuum state of the waveguide field, and $\mathcal{N} = e^{-|\alpha_{\mathrm{in}}|^2/2}$ is a normalization factor. The initial state of the qubit-cavity system at the initial moment $t = t_{\mathrm{i}}$ is $|\mathrm{g}, 0\rangle$. The initialization error of the qubit state is taken into account as a part of the readout errors ($\varepsilon_{\mathrm{r}}^{\mathrm{g}}$, $\varepsilon_{\mathrm{r}}^{\mathrm{e}}$). Therefore, the initial density matrix of the overall system is written as

$$\rho(t_{\mathrm{i}}) = |\mathrm{g}, 0\rangle\langle \mathrm{g}, 0| \otimes |\psi_{\mathrm{i}}\rangle\langle\psi_{\mathrm{i}}|. \tag{S8}$$

C. Time evolution

Throughout this study, we analyze the interaction between the input pulse mode and the qubit-cavity system in the Heisenberg picture. The Heisenberg equations for the system operators are obtained from Eq. (S3). For example,

a, σ_{ge} and σ_{ee} evolves as

$$\frac{d}{dt}a = [-i(\omega_{\mathrm{c}}+\chi)-\kappa_{\mathrm{tot}}/2]a + 2i\chi a\sigma_{\mathrm{ee}} - i\sqrt{\kappa_{\mathrm{ex}}}\widetilde{a}_{-t+t_{\mathrm{i}}}(t_{\mathrm{i}}) + \cdots, \tag{S9}$$

$$\frac{d}{dt}\sigma_{\mathrm{ge}} = (-i\omega_{\mathrm{q}} - \gamma_{\phi}^{\mathrm{tot}})\sigma_{\mathrm{ge}} + 2i\chi a^{\dagger}a\sigma_{\mathrm{ge}} + \cdots, \tag{S10}$$

$$\frac{d}{dt}\sigma_{\mathrm{ee}} = -\gamma_1\sigma_{\mathrm{ee}} + \gamma_2\sigma_{\mathrm{gg}} + \cdots, \tag{S11}$$

where $\kappa_{\mathrm{tot}} = \kappa_{\mathrm{ex}}+\kappa_{\mathrm{in}}$, $\gamma_1 = \gamma(1+n_{\mathrm{B}})$, $\gamma_2 = \gamma n_{\mathrm{B}}$, $\gamma_{\phi}^{\mathrm{tot}} = \gamma_{\phi}+(\gamma_1+\gamma_2)/2$, and the dots represent the contributions from the environmental vacuum fluctuations. We denote the expectation value of an operator $A(t)$ by $\langle A\rangle = \mathrm{Tr}\{A(t)\rho(t_{\mathrm{i}})\}$, where the initial density matrix is defined in Eq. (S8). From the property that a coherent state is an eigenstate of a field operator, we can rigorously replace $\widetilde{a}_r(t_{\mathrm{i}})$ with $\alpha_{\mathrm{in}}f_{\mathrm{in}}(r-t_{\mathrm{i}})$. Then, the operator equations (S9)–(S11) are recast into the following c-number ones,

$$\frac{d}{dt}\langle a\rangle = [-i(\omega_{\mathrm{c}}+\chi)-\kappa_{\mathrm{t}}/2]\langle a\rangle + 2i\chi\langle a\sigma_{\mathrm{ee}}\rangle - i\sqrt{\kappa_{\mathrm{ex}}}\alpha_{\mathrm{in}}f_{\mathrm{in}}(-t), \tag{S12}$$

$$\frac{d}{dt}\langle\sigma_{\mathrm{ge}}\rangle = (-i\omega_{\mathrm{q}} - \gamma_{\phi}^{\mathrm{tot}})\langle\sigma_{\mathrm{ge}}\rangle + 2i\chi\langle a^{\dagger}a\sigma_{\mathrm{ge}}\rangle, \tag{S13}$$

$$\frac{d}{dt}\langle\sigma_{\mathrm{ee}}\rangle = -\gamma_1\langle\sigma_{\mathrm{ee}}\rangle + \gamma_2\langle\sigma_{\mathrm{gg}}\rangle. \tag{S14}$$

Besides the above time evolution, the $Y/2$ and $-Y/2$ gates are applied to the qubit. We treat these gates simply as the instantaneous unitary transformations on the qubit operators. The $Y/2$ gate at $t = t_{\mathrm{i}}$ is written as

$$\begin{pmatrix} \sigma_{\mathrm{gg}} & \sigma_{\mathrm{ge}} \\ \sigma_{\mathrm{eg}} & \sigma_{\mathrm{ee}} \end{pmatrix} \to \frac{1}{2}\begin{pmatrix} \sigma_{\mathrm{gg}}+\sigma_{\mathrm{eg}}+\sigma_{\mathrm{ge}}+\sigma_{\mathrm{ee}} & -\sigma_{\mathrm{gg}}-\sigma_{\mathrm{eg}}+\sigma_{\mathrm{ge}}+\sigma_{\mathrm{ee}} \\ -\sigma_{\mathrm{gg}}+\sigma_{\mathrm{eg}}-\sigma_{\mathrm{ge}}+\sigma_{\mathrm{ee}} & \sigma_{\mathrm{gg}}-\sigma_{\mathrm{eg}}-\sigma_{\mathrm{ge}}+\sigma_{\mathrm{ee}} \end{pmatrix}, \tag{S15}$$

and the $-Y/2$ gate at $t = t_{\mathrm{g}}$ is written as

$$\begin{pmatrix} \sigma_{\mathrm{gg}} & \sigma_{\mathrm{ge}} \\ \sigma_{\mathrm{eg}} & \sigma_{\mathrm{ee}} \end{pmatrix} \to \frac{1}{2}\begin{pmatrix} \sigma_{\mathrm{gg}}-\sigma_{\mathrm{eg}}-\sigma_{\mathrm{ge}}+\sigma_{\mathrm{ee}} & \sigma_{\mathrm{gg}}-\sigma_{\mathrm{eg}}+\sigma_{\mathrm{ge}}-\sigma_{\mathrm{ee}} \\ \sigma_{\mathrm{gg}}+\sigma_{\mathrm{eg}}-\sigma_{\mathrm{ge}}-\sigma_{\mathrm{ee}} & \sigma_{\mathrm{gg}}+\sigma_{\mathrm{eg}}+\sigma_{\mathrm{ge}}+\sigma_{\mathrm{ee}} \end{pmatrix}. \tag{S16}$$

At the final moment $t = t_{\mathrm{f}}$, the qubit state is measured in the Z axis with the readout errors ($\varepsilon_{\mathrm{r}}^{\mathrm{g}}$, $\varepsilon_{\mathrm{r}}^{\mathrm{g}}$).

D. Quantum efficiency

By solving Eqs. (S12)–(S14) and similar equations for the terms such as $\langle a\sigma_{\mathrm{ee}}\rangle$ and $\langle a^{\dagger}a\sigma_{\mathrm{ge}}\rangle$, together with the qubit rotations of Eqs. (S15) and (S16), we calculate $P_{\mathrm{e}} = \langle\sigma_{\mathrm{ee}}(t_{\mathrm{f}})\rangle$ at the final moment t_{f}. Taking account of the readout errors, we obtain the qubit excitation probability as $\widetilde{P}_{\mathrm{e}} = \varepsilon_{\mathrm{r}}^{\mathrm{g}} + \langle\sigma_{\mathrm{ee}}(t_{\mathrm{f}})\rangle(1-\varepsilon_{\mathrm{r}}^{\mathrm{g}}-\varepsilon_{\mathrm{r}}^{\mathrm{e}})$. In Fig. 2b of the main text, we set $l = 500$ ns, $t_{\mathrm{i}} = -400$ ns, $t_{\mathrm{g}} = 400$ ns, and $t_{\mathrm{f}} = 500$ ns, as shown in Section S4.

The quantum efficiency of the single-photon detection and the dark-count probability are accessible by varying the average photon number $|\alpha_{\mathrm{in}}|^2$ in the input pulse mode. (Theoretically, this is automatically done by solving the evolution equations perturbatively in α_{in} and calculating the components of $\tilde{P}_{\mathrm{e}}$ proportional to $|\alpha_{\mathrm{in}}|^0$ and $|\alpha_{\mathrm{in}}|^2$.)

In Fig. S8, we show the dependence of the quantum efficiency on the system parameters, κ_{ex}, κ_{in}, γ, and γ_{ϕ}. The following parameters are fixed here: $\chi/2\pi = 1.5$ MHz, $n_{\mathrm{B}} = 0$, $l = 500$ ns, and $\varepsilon_{\mathrm{r}}^{\mathrm{g}} = \varepsilon_{\mathrm{r}}^{\mathrm{e}} = 0$. Considering the experimentally achieved values of $\kappa_{\mathrm{ex}}/2\chi = 1.1$, $\kappa_{\mathrm{in}}/2\chi = 0.083$, $\gamma/2\chi = 0.0014$, and $\gamma_{\phi}/2\chi = 0.0012$, we conclude that the quantum efficiency in the experiment is limited by the internal loss of the cavity.

E. Density matrix of output photon

Here, we outline the theoretical evaluation of the conditional/unconditional density matrix of the reflected pulse mode. We first introduce the mode function $f_{\mathrm{out}}(r)$ of the reflected pulse mode. For a long input pulse ($l \gg \kappa_{\mathrm{ex}}^{-1}$), the pulse envelope is almost unchanged after reflection except for the slight delay due to absorption and re-emission

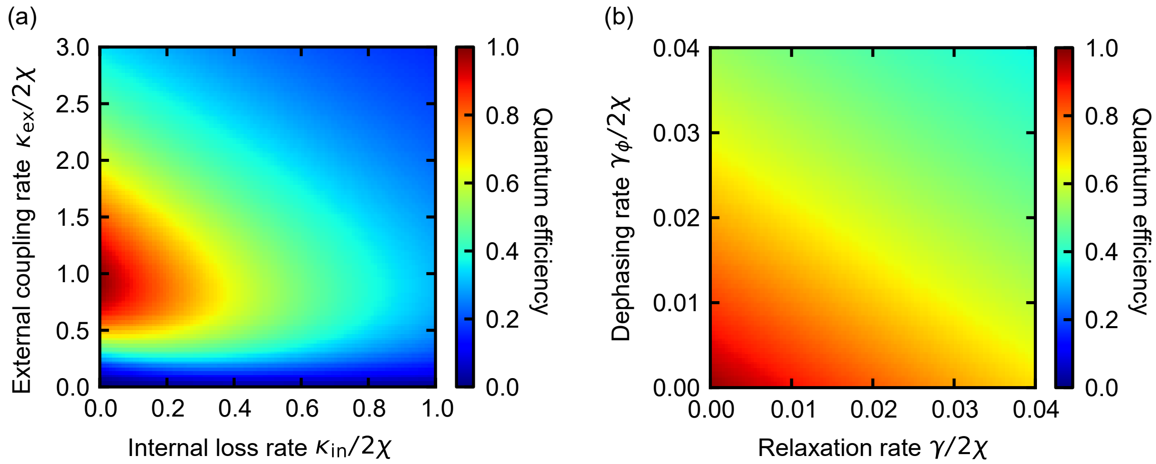

FIG. S8. Dependence of the quantum efficiency on the system parameters. (a) Quantum efficiency as a function of $\kappa_{\rm ex}$ and $\kappa_{\rm in}$. An ideal qubit ($\gamma = \gamma_\phi = 0$) is assumed here. (b) Quantum efficiency as a function of γ and γ_ϕ. The optimal cavity parameters $\kappa_{\rm ex} = 2\chi$ and $\kappa_{\rm in} = 0$ are used in accordance with the result in (a).

by the cavity. We therefore set $f_{\rm out}(r) = f_{\rm in}(r + \tau_d)$, where τ_d is the delay time of the order of $\kappa_{\rm ex}^{-1}$. Using this wavepacket, we define the creation operator $A^\dagger$ of the output photon (in the Heisenberg picture at time t) by

$$A^\dagger(t) = \int_0^{t-t_{\rm i}} dr\ f_{\rm out}(r-t)\widetilde{a}_r^\dagger(t). \tag{S17}$$

This operator satisfies the bosonic commutation relation of $[A, A^\dagger] = 1$.

For concreteness, we hereafter focus on the density matrix conditioned on the outcome of the qubit state ($q =$ g,e) at the final moment $t_{\rm f}$. This density matrix is determined from the moments of the field operators, $\langle \sigma_{qq}(t_{\rm f}) A^{\dagger m}(t_{\rm f}) A^n(t_{\rm f})\rangle$ ($m, n = 0, 1, \cdots$) [5]. In particular, when the reflected pulse mode contains up to one photon as in the current case, we need only three quantities, $P_q = \langle \sigma_{qq}\rangle$, $A_q = \langle \sigma_{qq} A\rangle$, and $N_q = \langle \sigma_{qq} A^\dagger A\rangle$. P_q can be calculated with the prescription presented in Section C. For calculation of A_q and N_q, which contain the output field operator ($\widetilde{a}_r$ with $r > 0$), we use the input-output relation,

$$\widetilde{a}_r(t) = \widetilde{a}_{r-t+t_{\rm i}}(t_{\rm i}) - i\sqrt{\kappa_{\rm ex}}\,a(t-r)\theta(r)\theta(t-t_{\rm i}-r), \tag{S18}$$

where θ is the Heaviside step function. A_q is recast into the following form,

$$A_q = \langle \sigma_{qq}(t)\rangle \times \alpha \int_{t_{\rm i}}^{t_{\rm f}} dt\ f_{\rm out}^*(-t) f_{\rm in}(-t) - i\sqrt{\kappa_{\rm ex}} \int_{t_{\rm i}}^{t_{\rm f}} dt\ f_{\rm out}^*(-t)\langle \sigma_{qq}(t_{\rm f}) a(t)\rangle. \tag{S19}$$

Similarly, up to the three-time correlation function is required for calculation of N_q. The elements of the conditional density matrix $\rho^{\rm q}$ are determined from P_q, A_q, and N_q by

$$\rho_{00}^q = \frac{P_q - N_q}{P_q}, \tag{S20}$$

$$\rho_{01}^q = \frac{A_q}{P_q}, \tag{S21}$$

$$\rho_{11}^q = \frac{N_q}{P_q}. \tag{S22}$$

Taking account of the readout errors, the conditional density matrix $\widetilde{\rho^q}$ are determined by

$$\widetilde{\rho^{\rm g}} = \frac{P_{\rm e}(1-\varepsilon_{\rm r}^{\rm e})\,\rho^{\rm e} + P_{\rm g}\varepsilon_{\rm r}^{\rm g}\,\rho^{\rm g}}{P_{\rm e}(1-\varepsilon_{\rm r}^{\rm e}) + P_{\rm g}\varepsilon_{\rm r}^{\rm g}}, \tag{S23}$$

$$\widetilde{\rho^{\rm e}} = \frac{P_{\rm g}(1-\varepsilon_{\rm r}^{\rm g})\,\rho^{\rm g} + P_{\rm e}\varepsilon_{\rm r}^{\rm e}\,\rho^{\rm e}}{P_{\rm g}(1-\varepsilon_{\rm r}^{\rm g}) + P_{\rm e}\varepsilon_{\rm r}^{\rm e}}. \tag{S24}$$

[1] A. A. Clerk and D. W. Utami, Phys. Rev. A **75**, 042302 (2007).
[2] J. Gambetta, A. Blais, D. I. Schuster, A. Wallraff, L. Frunzio, J. Majer, M. H. Devoret, S. M. Girvin, and R. J. Schoelkopf, Phys. Rev. A **74**, 042318 (2006).
[3] U. Leonhardt, *Measuring the Quantum State of Light* (Cambridge University Press, Cambridge, 1997).
[4] A. I. Lvovsky, Journal of Optics B: Quantum and Semiclassical Optics **6**, S556 (2004).
[5] V. Bužek, G. Adam, and G. Drobný, Physical Review A **54**, 804 (1996).